Disentangling Particle Composition to Improve Space-Based Quantification of POC in Optically Complex Estuarine and Coastal Waters

Mengyu Li, Fang Shen, Emanuele Organelli, Wei Luo, Renhu Li, Xuerong Sun, and Xiaodao Wei

***Abstract*— In estuarine-coastal-shelf seas, particulate organic carbon (POC) shows the highest turnover rates of any organic carbon pool on the planet, playing a key role in the biological carbon pump. Compared with open ocean, estuarine and coastal waters are affected by large river inputs and show high hydrodynamic variability, which results in a mixture of diverse particles that includes inorganic mineral particles, living algal particles, and organic detritus. The highly complex and variable particle compositions in estuarine-coastal-shelf waters pose significant challenges in assessing their distinct roles in the carbon cycle and total POC. To overcome challenges, we collected biogeochemical and optical in situ data from 2014 to 2020 in estuarine-coastal-shelf waters of eastern China, which is one of the largest estuarine-coastal-shelf systems in the world, to develop an algorithm that can optically discriminate particle composition and estimate their respective contributions to POC. The algorithm combines the quasi-analytical algorithm and the semi-empirical radiative transfer algorithm to estimate total suspended particle concentrations and the mass fraction of organic particles from which both phytoplankton- and detritus-related POC fractions are derived. Compared to existing POC algorithms, this algorithm shows improved retrievals compared to in situ counterparts, with r^2 and root mean squared error (RMSE) values of 0.84 and 16.57 μg L^{-1}, respectively. The algorithm is also applied to Sentinel-3/ocean and land color instrument (OLCI) images for the year of 2020. Applying the particle component discrimination method can enhance our understanding of the roles of different particle compositions in coastal carbon cycling affected by strong land-sea exchange.**

***Index Terms*— Inherent optical properties, particle composition, particulate organic carbon (POC), sentinel-3/ocean and land color instrument (OLCI).**

I. Introduction

PARTICULATE organic carbon (POC) refers to organic carbon associated with particles retained by GF/F filters with a pore size of 0.7 μm [1]. These particles, spanning a wide size range, include phytoplankton and organic detritus [2]. Phytoplankton and organic detritus are key actors of the ocean's biological carbon pump and sustain higher trophic levels [3], [4]. For example, living phytoplankton convert CO_2 to POC through photosynthesis, while nonliving organic detritus from terrestrial or marine sources can be gravitationally pumped and buried in the seafloor [5]. Recognizing the composition and contribution of diverse particle types within the marine POC pool is, therefore, crucial for accurate estimation of the ocean's carbon budget [6].

Estuarine-coastal-shelf waters, influenced by large river plumes and adjoining oceanic processes, exhibit spatial and temporal variations in particle concentration, composition, and then their contributions to POC [7], [8]. Particle concentration gradually decreases in the seaward direction after reaching its peak in the turbidity maximum zone (TMZ). Comparatively, there have been few reports on the particle composition in estuarine-coastal-shelf waters. In estuaries and nearshore waters, the reported dominant components are biological detritus and mineral sediments brought by the river. Outside the TMZ in the seaward direction, the dominant components are phytoplankton and their derived particles [9], [10]. These factors result in significant spatial and temporal changes in particle characteristics in this area, like particle composition, which yield complexity in the optical properties of the surrounding waters [11].

Because marine particles scatter and absorb light, remotely sensed optical measurements are crucial for monitoring suspended particles and POC in dynamic estuarine-coastal-shelf seas, where particle characteristics and distributions vary extensively [12], [13]. The high turbidity and the optical complexity of estuarine-coastal-shelf waters, however, pose challenges to using optical methods to invert mineral particles, phytoplankton and organic detritus proportions, and contributions of phytoplankton and organic detritus to POC pool [14], [15]. The development of innovative approaches is, therefore, needed to improve the reliability of POC estimation by untangling the complexity of particle composition in these waters.

Existing bio-optical algorithms for estimating POC using satellite ocean color remote sensing have primarily been developed for open ocean waters [16], [17], [18]; however, applying these algorithms to estuarine-coastal-shelf waters, where phytoplankton is not the main contributor to POC,

Manuscript received 5 November 2023; revised 6 December 2023; accepted 7 December 2023. Date of publication 12 December 2023; date of current version 26 December 2023. This work was supported by the National Science Foundation of China Projects under Grant 42271348 and Grant 42076187. The work of Mengyu Li was supported by the China Scholarship Council for the Joint Ph.D. Program through the Institute of Marine Sciences (ISMAR) of the National Research Council (CNR), Italy, under Grant 202206140082. *(Corresponding author: Fang Shen.)*

Mengyu Li, Fang Shen, Wei Luo, Renhu Li, Xuerong Sun, and Xiaodao Wei are with the State Key Laboratory of Estuarine and Coastal Research (SKLEC), East China Normal University, Shanghai 200241, China (e-mail: fshen@sklec.ecnu.edu.cn).

Emanuele Organelli is with the National Research Council (CNR), Institute of Marine Sciences (ISMAR), 00133 Rome, Italy.

This article has supplementary downloadable material available at https://doi.org/10.1109/TGRS.2023.3341462, provided by the authors.

Digital Object Identifier 10.1109/TGRS.2023.3341462

TABLE I

BRIEF DESCRIPTIONS OF THE IN SITU DATASETS IN THIS STUDY, YRE, YS, BS, AND ECS REPRESENT THE YANGTZE RIVER ESTUARY, THE YELLOW SEA, THE BOHAI SEA, AND THE EAST CHINA SEA, RESPECTIVELY

Data	Sampling time	Sampling regions	Sites	Collected samples						
				TSM	$b_{bp}(\lambda)$	$R_{rs}(\lambda)$	$a_{ph}(\lambda)$ $a_{NAP}(\lambda)$	$a_g(\lambda)$	OSM ISM	POC
Historic dataset from Wei *et al.* [13]	2014-2015	YRE, YS, BS, ECS	493	512	396	208	89	89	-	512
New dataset from cruises in 2020	May 2020 July 2020	BS, YS, YRE	107	107	88	77	107	107	107	-

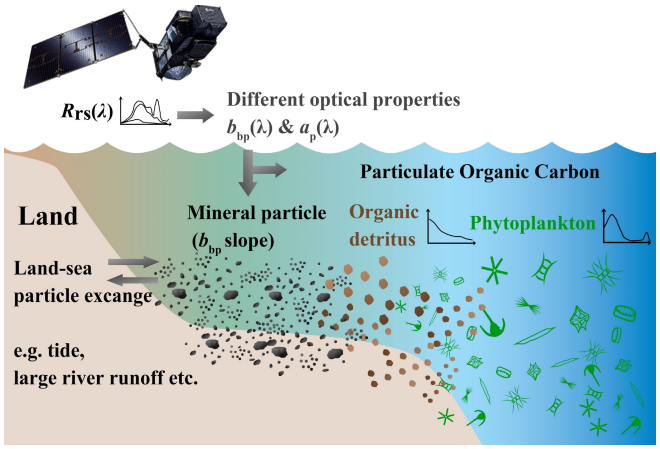

Fig. 1. Overview of the idea proposed in this study. Organic and inorganic components can be separated based on the difference in optical backscattering properties. Then, organic detritus and phytoplankton can be differentiated based on the light absorption coefficients. Subsequently, the relationships between organic-detritus/phytoplankton and their POC contributions are established, and further to approach total POC.

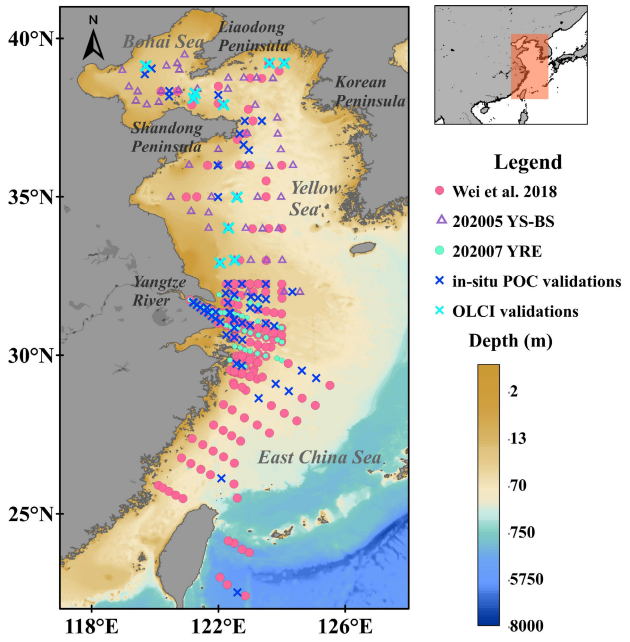

Fig. 2. In situ sampling locations of the in situ datasets. The pink circle, purple triangle, and light blue circle represent the Wei et al. [13] dataset, the 2020 YS-BS, and YRS cruises, respectively. The blue and light blue crosses represent the in situ POC validation station and the satellite validation station, respectively. The coastline is downloaded from SOEST, while bathymetry maps are from the ETOPO1, version 4.3.1.

leads to significant estimation errors. Previous attempts to improve POC retrieval in coastal areas have focused on water classification and local bio-optical models [12], [13], [19]. These approaches not only have limited applicability across varying conditions but also fail to capture the contributions of different particle components to the carbon cycle.

This study innovatively addresses the challenge of discerning particle composition in optically complex waters, such as in Chinese seas, and of assessing the contribution of different particle types to the POC pool. An overview of the proposed idea is shown in Fig. 1. To achieve this, we compiled a comprehensive in situ database of biogeochemical and optical parameters. By refining existing inversion algorithms, namely the quasi-analytical algorithm (QAA, Lee et al. [20]) and the semi-empirical radiative transfer (SERT, Shen et al. [9], [21]), we estimated the total suspended particle concentration and particle inherent optical properties using in situ remote sensing reflectance. Leveraging the QAA-derived particle backscattering spectral slope, we retrieved the mass fraction of organic particles and combined it with QAA-derived particulate light absorption coefficients to quantify the contributions of phytoplankton and detritus to the POC pool. This approach is further applied to Sentinel-3 ocean and land color instrument (OLCI) data to showcase POC variations in the Chinese seas. The results of this work provide a first synoptic view of the spatial distribution of the POC contributions from different sources and particle components in estuarine-coastal-shelf waters, thus filling the knowledge gap between the contribution of different particle sources and compositions to the nearshore carbon cycle.

II. MATERIAL AND DATA

A. In Situ Dataset

The in situ dataset includes field cruises carried out in 2020 together with the historical dataset compiled by Wei et al. [13]. (The main parameters used in this study and their brief descriptions are shown in the Appendix. See Table I for the brief dataset description). All the locations of in situ measurements and validations are shown in Fig. 2. All sampling and measurement methods are the same for the two datasets, following the same processes and protocols.

The field cruises in 2020 were carried out in estuarine-coastal-shelf waters of eastern China, e.g., in the Bohai Sea (BS) and Yellow Sea (YS) in May, and the Yangtze River Estuary (YRE) in July, collected samples in 107 stations. Measurements included simultaneous measurements of

the particulate optical backscattering coefficients (b_{bp}, m^{-1}), phytoplankton and nonalgal absorption coefficients (a_{ph} and a_{NAP}, respectively, m^{-1}), chromophoric dissolved organic matter (CDOM) light absorption coefficient (a_g, m^{-1}), organic suspended matter mass fraction (OSM, %), remote sensing reflectance (R_{rs}, m^{-1}), and total suspended particulate matter (TSM, g L^{-1}). The historical dataset of Wei et al. [13] included data acquired in the YRE, YS, BS, and East China Sea (ECS) during the period from 2014 to 2015. This dataset is composed by simultaneous measurements for 208 measurements of R_{rs}, b_{bp}, TSM, particulate absorption coefficient (a_p, m^{-1}), a_g, and POC.

1) Water Sampling: Surface water was collected from 3 m depth using a rosette system equipped with Niskin bottles and a conductivity-temperature-depth profiler (CTD, Seabird 911). For a_p, seawater (0.1–3 L) was filtered onto Whatman GF/F Glass Microfiber Filters (pore size: 0.7 μm, diameter: 25 mm) under low vacuum pressure onboard, while some filters were stored as blank, following the NASA ocean optics protocols [22]. For samples collected to analyze particle characteristics (TSM, POC, and organic suspended matter mass fraction), seawater (1 − 4 L determined according to water turbidity) was filtered on prerinsed, precombusted, and preweighed Whatman GF/F Glass Microfiber Filters (pore size: 0.7 μm, diameter: 47 mm) under low vacuum pressure [22], [23]. For the analysis of the CDOM, the water was sampled through filtration on board using Millipore polycarbonate membrane, (pore size: 0.22 μm, diameter: 47 mm) under low vacuum immediately after sampling, into the presoaked and precombusted borosilicate glass vials according to Pegau et al. [24]. All particle samples were stored in the −40 °C cleaned refrigerator until analysis when back at the laboratory.

2) Optical Measurements:

a) Light absorption properties: $a_p(\lambda)$, $a_{ph}(\lambda)$, and $a_{NAP}(\lambda)$ (see Table V) were measured with a PerkinElmer Lambda 1050 UV/VIS spectrophotometer equipped with a 15 cm integrating sphere in the laboratory, inside the sphere within the range 200–1000 nm at 2 nm resolution and 1 nm interpolation, following the NASA and IOCCG ocean optics protocols [24], [25]; $a_{ph}(\lambda)$ and $a_{NAP}(\lambda)$ were determined using the method proposed by Röttgers and Gehnke [26], subtracting measurements acquired after pigment extraction in methanol from a_p; a_g were measured from 250 to 900 nm using a 10 cm quartz cuvette referenced to the Milli-Q water by the PerkinElmer Lambda 1050 UV/VIS spectrophotometer, after being unfrozen and warmed to room temperature under fully dark conditions; $a_g(\lambda)$ was then obtained according to the method proposed by Pegau et al. [27].

b) Optical backscattering properties: The volume scattering function $\beta(\lambda, \theta)$ at a single angle in the backward direction, $\theta = 124°$, was collected at nine wavelengths (412, 440, 488, 510, 532, 595, 650, 676, and 715 nm) with WetLabs ECO BB9 meter between 0 and 5 m. Raw data were processed according to the ocean optics protocols [28]. $\beta(\lambda, \theta)$ was obtained according to the users' manual [29]. b_{bp} (λ) was estimated from $\beta(\lambda, \theta)$ as

$$b_{bp}(\lambda) = 2\pi\chi_p(124°)[\beta(\lambda, 124°) - \beta_w(\lambda, 124°)] \quad (1)$$

where $\chi_p(124°)$ is a spectrally independent nondimensional factor that relates the particulate backscattering coefficient to volume scattering at 124° in the backward direction [30], [31], [32], and $\beta_w(\lambda, 124°)$ is the volume scattering coefficient of seawater [33], [34]. Based on Sullivan et al. [35], it was used $\chi_p(124°) = 1.076$.

c) Remote sensing reflectance: In situ $R_{rs}(\lambda)$ spectra were derived from above water measurements of sea surface upwelling radiance (L_{tot}), downwelling sky radiance (L_s), and downwelling solar irradiance (E_d) from 350 to 900 nm with 1 nm interval acquired by the Hyperspectral Surface Acquisition System (HyperSAS, Sea-Bird Scientific Inc.). $R_{rs}(\lambda)$ was obtained as follows:

$$R_{rs}(\lambda) = \frac{L_{tot}(\lambda) - \rho_{sky}(\lambda)L_{s,sky}(\lambda)}{E_d(\lambda)} \quad (2)$$

where L_{tot} is the sea surface upwelling radiance, $L_{s,sky}(\lambda)$ is the sky incoming spectral radiance, and $\rho_{sky}(\lambda)$is the sky radiance spectral reflectance. $L_s = \rho_{sky}(\lambda)\ L_{s,sky}(\lambda)$. The spectral optimization approach was applied to remove surface-reflected skylight [36]. The details are described in Shen et al. [37] and Sokoletsky and Shen [38]. The range of $R_{rs}(\lambda)$ features used in this work is shown in Fig. 3.

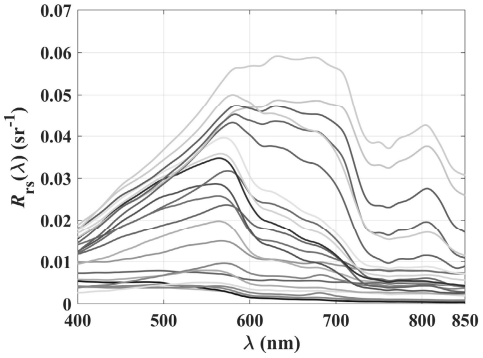

Fig. 3. Typical spectra of $R_{rs}(\lambda)$ collected in this work.

3) Particle Characteristics: TSM samples were gravimetrically analyzed, as outlined in Strickland and Parsons [23] and Neukermans et al. [39]. The filters were gently washed in the laboratory with MilliQ water to remove friable fractions and then dried at 75 °C for 1 h. Then they were weighed on a balance to record the initial weight (w_1) with a precision of 0.01 mg. Seawater samples were filtered after collection to record the volume (V). Then, the filters and funnel were gently washed with MilliQ water after filtration to remove salt and then stored in darkness at −20 °C. After the cruise, samples were dried at 75 °C until the weight got stable and then weighed after they were put in glassware for ≥4 h to cool at 45 °C. Then, the samples were weighed on the same balance to obtain w_2, from which total suspended matter (TSM) was calculated with $(w_2–w_1)/V$.

The particle composition was determined by the loss-on-ignition method [40]. To obtain inorganic suspended matter

mass fraction (ISM, %) and organic suspended matter mass fraction (OSM, %), the weighted filters were subsequently placed in a muffle furnace at 550 °C for more than 4 h until the weight unchanged with an accuracy of 0.01 mg, and then all the organic materials were assumed to be combusted. The filters were reweighed to obtain ISM, and the difference between TSM and ISM yielded the concentration of OSM [41].

The particulate volume concentration across different sizes was collected using the LISST-200X particle size analyzer (Sequoia Scientific Inc.). The collected raw data with a clean water background were processed by the LISST-200X software into volume concentration for $1 - 500$ μm 36 size classes [42].

In situ POC concentrations (μg L^{-1}) were determined in the laboratory following the Joint Global Ocean Flux Study measurement protocols [43]. Samples were dried and acidified to remove carbonates [44], then dried again for measuring organic carbon using the elemental analyzer (Vario EL-III, Elementar, Germany). A similar analysis was done to determine the background organic carbon content on unused (blank) precombusted filters from the same batch of filters that were used to prepare samples.

B. Satellite Data and Processing

Sentinel-3/OLCI Level-1B full-resolution images (OL_1_EFR, 300 m) were collected from the European Space Agency Copernicus Open Access Hub (https://scihub.copernicus.eu/dhus/#/home). We used the Case 2 Regional Coast Color (C2RCC) algorithm atmospheric correction processor in the European Space Agency (ESA) Sentinel-3 toolbox. The algorithm is based on an artificial neural network inversion model to derive water-leaving radiance and in-water optical properties [45], which is more applicable in the China Shelf Sea [46], (see Supplement document, Fig. S1, and Table S1 for detailed comparisons and validations). Algorithm information can be obtained at https://c2rcc.org/.

C. Error Tests

The performance of the proposed model to detect POC and its phytoplankton and organic detrital components in estuarine-coastal-shelf waters (see Sections III and IV) was quantified using the coefficient of determination (R^2), mean absolute percentage error (MAPE), and root mean squared error (RMSE), calculated between in situ measurements and model-derived estimates as follows:

$$\mathrm{R}^2 = 1 - \frac{\sum_{i=1}^{N}\left(X_{i,E} - X_{i,M}\right)^2}{\sum_{i=1}^{N}\left(X_{i,M} - \overline{X_{i,M}}\right)^2} \tag{3}$$

$$\mathrm{MAPE} = \frac{1}{N}\sum_{i=1}^{N}\left|X_{i,\mathrm{E}} - X_{i,\mathrm{M}}\right| \tag{4}$$

$$\mathrm{RMSE} = \left[\frac{1}{N}\sum_{i=1}^{N}\left(X_{i,\mathrm{E}} - X_{i,\mathrm{M}}\right)^2\right]^{1/2} \tag{5}$$

where N is the number of samples, X is the IOPs, TSM or POC, E and M represent estimated and measured variables, respectively.

III. Method Development

A flowchart of the method and processing procedures applied in this study is shown in Fig. 4, which includes tuning the QAA and SERT algorithm described in Sections III-A and III-B to obtain $b_{\mathrm{bp}}(\lambda)$, γ, $a_{\mathrm{ph}}(\lambda)$, $a_{\mathrm{NAP}}(\lambda)$ and TSM from $R_{\mathrm{rs}}(\lambda)$. In addition, the relationship between OSM and $b_{\mathrm{bp}}(\lambda)$ spectral slope γ in Section III-C, the distinction between phytoplankton and organic detritus particles, and the estimation of their POC contributions to the total POC concentration in Section III-D, have been explored.

A. QAA Tuning

The QAA is a semi-analytical algorithm that derives IOPs such as spectral light absorption and backscattering coefficients from r_{rs}, originally developed by Lee et al. [20] and now updated into the sixth version (QAA_v6). QAA_v6 is mainly applicable to the open ocean, and thus, there are still large uncertainties in deriving optical properties for optically complex waters [14], [47], [48]. Hence Wang et al. [14] developed a new QAA algorithm (QAA_Wang) based on QAA_v6, which was specifically designed for turbid and optically complex estuarine and coastal waters. In this study, a total of 161 synchronous optical measurements were used to recalibrate the empirical steps (S2 and S7 in Fig. 5). Instead of using the holdout cross-validation to divide data into 70% training and 30% validation, the k-fold method powered by MATLAB R2020b was used.

This work is mainly based on QAA_Wang algorithm (Wang et al. [14, Table 3]), and Step 9 in this work is from Step 9 in QAA_v6. Fig. 5 shows the algorithm flow based on QAA_Wang in this study. In Step 4 of the original QAA_Wang algorithm, the relation between $b_{\mathrm{bp}}(\lambda)$ slope γ and single-band b_{bp} shows low R^2 at 0.22, which may lead to low accuracy in estimating γ [14]; therefore, a two-band algorithm is introduced here to obtain γ [49].Then, the coefficients in Step 7 are updated with in situ measurements. In addition, in Step 9, an assumption of $a_{\mathrm{g}}(682)$ based on in situ data is introduced to calculate a_{ph}. Above all, the relationship of each variable in the updated is shown in Fig. 6, while the detailed coefficients and formulas are shown in Table II.

First, with $\lambda_0 = 490$ nm as the optimal reference wavelength, the values of $a_{\mathrm{nw}}(665)$ and $a_{\mathrm{nw}}(682)$ show a high correlation with $R_{\mathrm{rs}}(665)/R_{\mathrm{rs}}(490)$ and $R_{\mathrm{rs}}(682)/R_{\mathrm{rs}}(490)$, respectively [$R^2$ is 0.87, Fig. 6(a) and (b)], while the detailed equations and coefficients are shown in Table II. Then, $b_{\mathrm{bp}}(665)$ and $b_{\mathrm{bp}}(682)$ are obtained according to the analytical Step 3. $b_{\mathrm{bp}}(\lambda)$ is spectrally dependent and can be fit to the power function: $b_{\mathrm{bp}}(\lambda) = b_{\mathrm{bp}}(\lambda_0)(\lambda/\lambda_0)^{-\gamma}$, where λ_0 is the reference wavelength, and γ is the dimensionless spectral slope, γ can be analytically derived as Step 4 shown in Table II. The b_{bp} slope 665–682 ranged from 0 to 2.78 (Supplement document, Fig. S2). Then the empirical relationship of $a_{\mathrm{p}}(443)$ and $b_{\mathrm{bp}}(682)$ has been tuned with in situ data and is shown in Fig. 6(c) with high correlation coefficients with R^2 as 0.86. In Step 8 of QAA_Wang, $a_{\mathrm{dg}}(\lambda)$ is obtained. According to the in situ CDOM spectrum, the in situ measurements of $a_{\mathrm{g}}(682)$ are relatively stable, the average of the

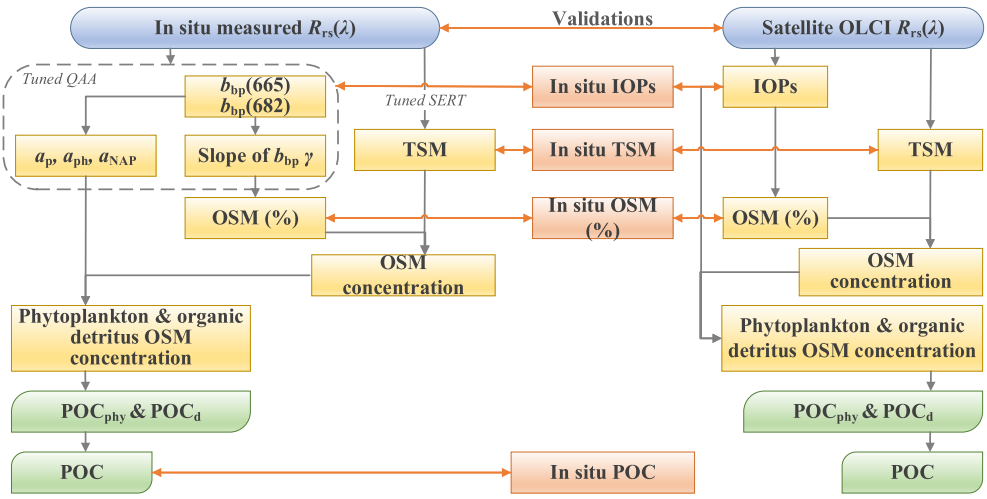

Fig. 4. Flowchart of the method and processing procedures developed in this study. The blue boxes represent inputs, the yellow boxes represent processes, the green boxes represent the output parameters, and the orange boxes represent validations.

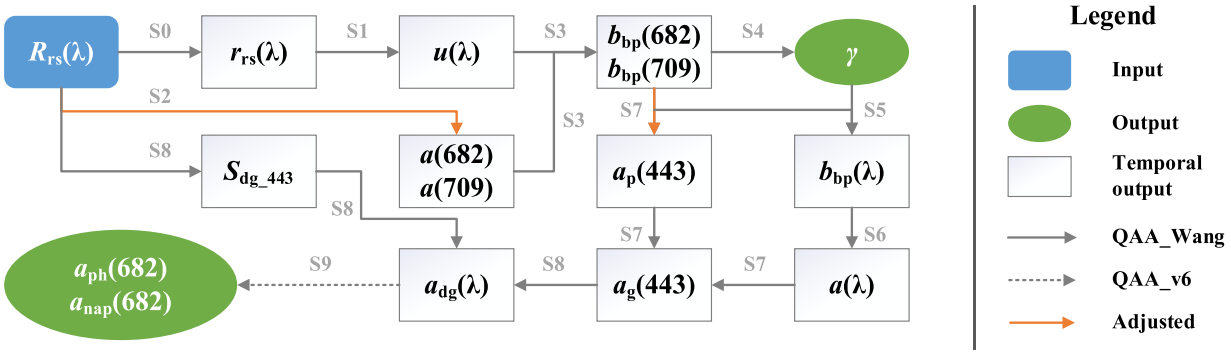

Fig. 5. Flowchart of the tuning QAA algorithm for estimating $a_{ph}(\lambda)$ and $a_{nap}(\lambda)$ from $R_{rs}(\lambda)$. Step numbers are denoted as S. The solid lines show the steps from QAA_Wang, while the dotted lines are the steps from QAA_v6. The orange lines represent the empirical steps recalibrated with in situ data.

TABLE II
DETAILED QAA EQUATIONS OF THE TUNING APPLIED IN THIS STUDY FOR OPTICALLY COMPLEX WATERS

Steps	Derivation	Property
Step 2	$a_{nw}(665) = 1.0317x^3 - 1.5253x^2 + 0.7748x - 0.0803$, $x = R_{rs}(665)/R_{rs}(490)$ $a_{nw}(682) = 0.9311x^3 - 1.3086x^2 + 0.6103x - 0.0470$, $x = R_{rs}(682)/R_{rs}(490)$	$a_{nw}(665)$ and $a_{nw}(682)$
Step 4	$\gamma = \ln[b_{bp}(665)/b_{bp}(682)]/\ln(665/682)$	γ
Step 7	$a_p(443) = 1.3559\ b_{bp}(682)^{0.5858}$	$a_p(443)$

TABLE III
α AND β CONSTANTS FOR SENTINEL-3/OCLI IN THE SERT MODEL. THE BOLD ANNOTATIONS REPRESENT THE BANDS AND THEIR R^2 USED IN THIS STUDY

Bands	α	β	R^2 ($N = 140$)
510	0.0423	337.3	0.697
560	0.0581	184.6	0.762
620	0.0770	52.79	**0.828**
665	0.0814	39.07	**0.827**
674	0.0816	37.88	**0.825**
682	0.0820	37.27	**0.825**
709	0.0808	28.25	**0.816**

219 measurements is 0.0045 m^{-1}, and the standard deviation is 0.0029 m^{-1}, with less than 10% influence on in situ $a_p(\lambda)$. Thus, the average value of $a_g(682)$ was used to participate in the calculation.

By using the independent validation dataset, the performance of the tuned QAA was evaluated and compared with independent in situ measurements, together with the results of error statistics. In general, the estimates compared reasonably well with independent in situ observations (Fig. 7, all $p < 0.01$). For the QAA algorithm, R^2 are 0.89 and 0.88, respectively, observed for $b_{bp}(665)$ and $b_{bp}(682)$ estimates, with RMSE at 0.02 [Fig. 7(a) and (b)]. It can be observed that there is overestimation in the low values of the two bands, as well as underestimation in the high values; however, γ is calculated using two highly correlated bands, which can effectively mitigate error propagation resulting from the estimation error of a single band, thus reducing the impact on γ estimation and subsequent OSM calculations. R^2 value

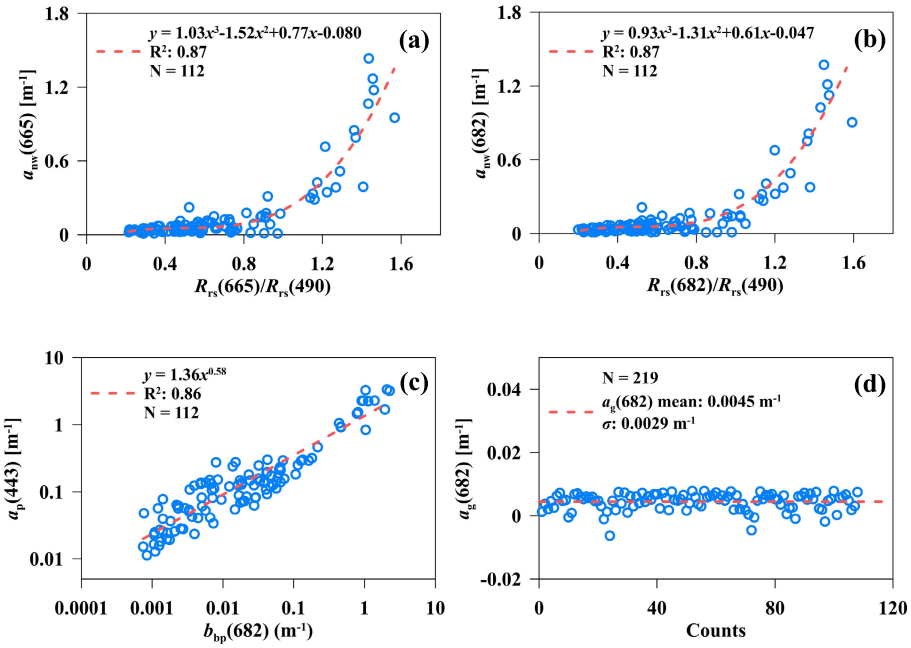

Fig. 6. Tuning of QAA empirical steps using in situ optical measurements for the Chinese optically complex waters. (a) $R_{rs}(665)/R_{rs}(490)$ versus $a_{nw}(665)$ for S2 in Fig. 5, (b) $R_{rs}(682)/R_{rs}(490)$ versus $a_{nw}(682)$ for S2, (c) $b_{bp}(682)$ versus $a_p(443)$ for S7 in Fig. 5, and (d) $a_g(682)$ in situ measurements and the average value at 0.0045 m^{-1}.

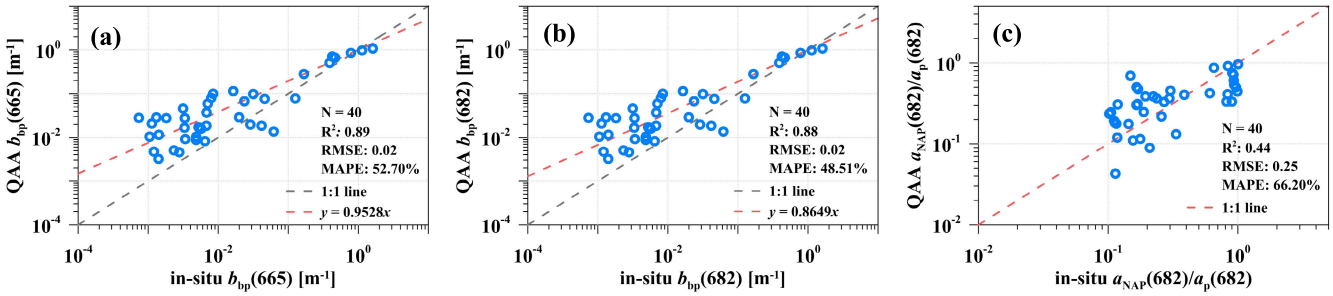

Fig. 7. (a) In situ measured $b_{bp}(665)$ versus estimated b_{bp} (665) from $R_{rs}(\lambda)$ by QAA. (b) In situ measured $b_{bp}(682)$ versus estimated b_{bp} (682) from $R_{rs}(\lambda)$ by QAA. (c) In situ measured $a_{NAP}(682)/a_p(682)$ versus estimated $a_{NAP}(682)/a_p(682)$ from $R_{rs}(\lambda)$ by QAA. The gray dashed lines represent the 1:1 line.

of 0.44 ($p < 0.01$) is observed for the $a_{NAP}(682)/a_p(682)$, with estimations distributed along the 1:1 line and MAPE and RMSE of 66.20% and 0.25%, respectively [Fig. 7(c)]. $a_p(443)$ validation is in Supplement document, Fig. S3, with RMSE of 0.1321 m^{-1} and MAPE of 59.33%.

B. SERT Tuning

The SERT model [9], [37] is expressed as

$$\mathrm{TSM} = \frac{2\alpha R_{rs}(\lambda)}{\beta\left[\alpha - R_{rs}(\lambda)\right]^2} \tag{6}$$

where the unit of the TSM is g/L and coefficients α and β vary with wavelengths. To apply the algorithm on Sentinel 3 OLCI, in situ R_{rs} data are simulated according to OLCI wave bands to obtain α and β. A total of 200 matched TSM and $R_{rs}(\lambda)$ data were collected, with 140 samples (70%) selected randomly as the training dataset, leaving 60 independent samples (30%) for validation. The α and β are given in Table III. The R_{rs} at 620–709 nm are selected ($R^2 > 0.8$) in this work for the multiband switching strategy of SERT in turbid waters to avoid reflectance saturation and maintain sensitivity to TSM variation.

The independent validation dataset ($N = 40$) was used, and the performance of the SERT model with original parameters ($\mathrm{SERT_{or}}$) and the recalibrated SERT algorithm for Sentinel-3/OLCI ($\mathrm{SERT_{OLCI}}$) for estimating TSM was evaluated and compared with the in situ measurements (Fig. 8). In general, the $\mathrm{SERT_{OLCI}}$ performs better than the SERT model with the original two parameters. TSM calculated by the original SERT model is overall higher than the measured data. For the $\mathrm{SERT_{OLCI}}$ algorithm, a high agreement is found with R^2 of 0.91 ($N = 40$), while the points are distributed along the 1:1 line.

C. Particle Type Differentiation

To estimate the quantity of organic matter in POC, we need first to exclude inorganic mineral particles from TSM. Further, living phytoplankton and organic detritus can be classified from the OSM. The inherent optical properties of suspended particles in natural waters vary widely, providing optical clues

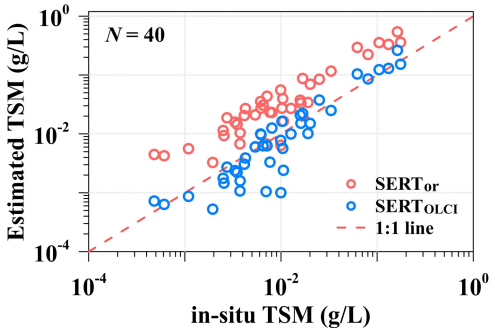

Fig. 8. In situ TSM versus estimated TSM using the SERT algorithm proposed by Shen et al. [9] and adapted to Sentinel-3/OLCI bands. The red circles represent the TSM calculated based on the original parameters, while the blue circles represent the estimated TSM based on the tuned algorithm for Sentinel-3/OLCI in this study.

to distinguish different particle types once mass concentration information has been removed [50], [51]. Thus, here, the spectral slope of $b_{bp}(\lambda)$, γ, has been proposed as an indicator of the particle composition in the coastal environment [11], [52], [53].

We used simultaneous γ and OSM proportion data of 77 stations in the dataset and randomly divided them into modeling and validation datasets in 1:1 ratio. Data pairs of 38 points are applied for analyzing the relationship between γ and OSM proportion [Fig. 9(a)]. The independent validation dataset ($N = 38$) was used to evaluate the OSM proportion estimated from the IOPs and compared with the in situ data in Fig. 9(b), with the error statistics results shown together. The relationship between OSM proportion and γ was identified as

$$p - \mathrm{OSM} = 0.22\gamma^{4.06} (R^2 = 0.81, N = 39). \quad (7)$$

In Fig. 9(a), OSM proportion was significantly correlated with γ ($R^2 = 0.81$) and increased as γ increased. The correlation between estimates and measured data for the OSM percentage [Fig. 9(b)] is significant ($p < 0.01$) with R^2 equal to 0.74 and low MAPE and RMSE (66.20% and 0.24%, respectively).

D. Organic-Particle-Type-Based POC Estimation

After the separation of OSM from TSM, OSM needs to be further divided into phytoplankton and organic detritus components, since the contribution of each component to POC may be different. Although natural water particles are extremely complex, here it is assumed that the primary contribution to POC comes from phytoplankton during the phytoplankton bloom. In estuaries with low phytoplankton content and in the TMZ, it can be assumed that the contribution to POC is primarily from organic detritus. It is, therefore, necessary to select representative in situ measurements with POC dominated by phytoplankton and organic detritus to establish the relationships between the each POC contributing components and OSM.

To distinguish between in situ stations where POC is primarily contributed by phytoplankton from those where organic detritus is the main contributor, it is necessary to introduce Q_{bbe} (backscattering efficiency). $Q_{bbe}(\lambda)$ indicates the dominant particle composition [54]. Q_{bbe} values in a typical phytoplankton environment (in the laboratory or algal bloom) are reported less than 0.01 [55], [56]. Q_{bbe} in the near-bottom layer or in the coast and estuary dominated by mineral and organic detritus is significantly greater than phytoplankton by two orders of magnitude [57]. Based on this, POC at stations with $Q_{bbe}(682)$ less than 0.01 were classified as primarily contributed by phytoplankton, while stations with $Q_{bbe}(682)$ greater than 1 were classified as primarily contributed by organic detritus, others were classified as POC contributed by mixed particles.

Assuming the particles were spherical [52], $Q_{bbe}(\lambda)$ was calculated as follows [58], [59]:

$$Q_{bbe}(\lambda) = b_{bp}(\lambda)/ac \quad (8)$$

where ac is particle cross-sectional area concentration, which can be obtained according to Wang et al. [59]. Overall, the results show a total of 31 stations with $Q_{bbe}(682)$ less than 0.01, and 44 stations with $Q_{bbe}(682)$ more than 1 (the locations of each category are shown in the Supplement document Fig. S4). For each component, 21 and 30 stations of POC were randomly selected from each category, respectively (90% of total selected station), as representative of the phytoplankton ($\mathrm{POC_{phy}}$) and organic detritus ($\mathrm{POC_d}$) contributions to POC. The contribution of phytoplankton and detritus OSM mass to POC was then calculated separately ($R^2 = 0.44$ for $\mathrm{POC_{phy}}$, $N = 21$; $R^2 = 0.87$ for $\mathrm{POC_d}$, $N = 30$; Fig. 10).

For mixed particle situation ($0.01 \le Q_{bbe}(682) \le 1$), $a_{ph}(\lambda)$ peak of chlorophyll-a (Chl$a$) at 682 nm and $a_{NAP}(\lambda)$ to determine the proportion of $a_p(\lambda)$. Because of the different optical signatures between phytoplankton and organic detritus related to phytoplankton pigments, $a_{NAP}(\lambda)/a_p(\lambda)$ and $a_{ph}(\lambda)/a_p(\lambda)$ at about 682 nm are very different. For the case of nonalgal particles dominated waters, $a_p(682)$ and $a_{NAP}(682)$ of those samples almost coincide, while there is a large difference between $a_p(682)$ and $a_{NAP}(682)$ in phytoplankton-dominated samples. This is used to distinguish the contribution percentage of various component OSM contents to POC at stations characterized by mixed particle composition. By combining the relationships established for each component OSM contribution to POC, we calculate the total POC content. Thus, the total POC is then computed as follows:

$$\mathrm{POC_t} = \mathrm{POC_{phy}} + \mathrm{POC_d}, \text{ where } \mathrm{POC_{phy}} = 76.242\mathrm{OSM_{phy}^{0.27}}$$
$$\mathrm{POC_d} = 37.324\mathrm{OSM_d^{0.95}} \quad (9)$$

while $\mathrm{OSM_{phy}}$ and $\mathrm{OSM_d}$ were obtained from the fraction of $a_{NAP}(\lambda)/a_p(\lambda)$ and $a_{ph}(\lambda)/a_p(\lambda)$, which provides the contribution percentage of each component to the OSM.

The randomly selected samples (10 for $\mathrm{POC_{phy}}$; 14 for $\mathrm{POD_d}$; 60 for POC) are used for validation (10% of total selected stations). Most points are distributed across the 1:1 line (Fig. 11). Fig. 11(a) shows the validation result of $\mathrm{POC_{phy}}$ estimation, with $R^2 = 0.41$ ($N = 10$, $p < 0.01$). The comparison between $\mathrm{POC_d}$ estimation and in situ measurements is shown in Fig. 11(b), with $R^2 = 0.74$ ($N = 14$, $p < 0.01$). For the validation of total POC estimation shown in Fig. 11(c), R^2 is 0.71 ($N = 60$, $p < 0.01$).

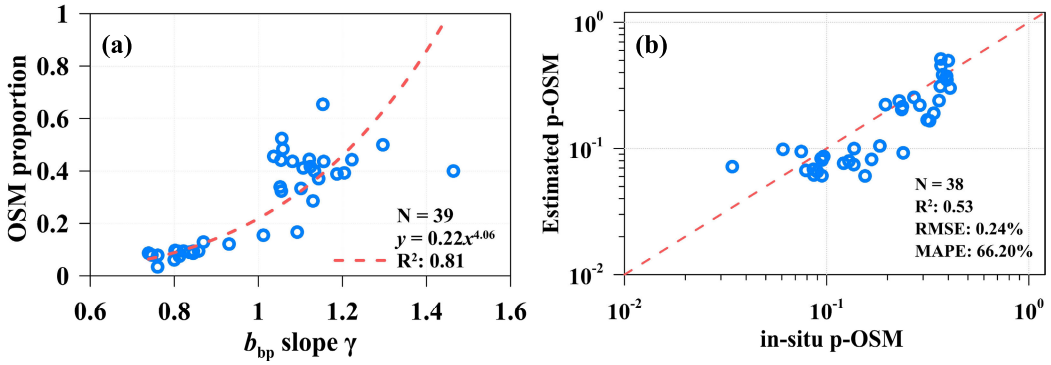

Fig. 9. (a) Relationships between the OSM proportion and the $b_{bp}(\lambda)$ spectral slope γ. The dotted red line indicates the fit curve. (b) In situ measured OSM concentration percentage versus estimated OSM concentration percentage. The red dashed line indicates the 1:1 line.

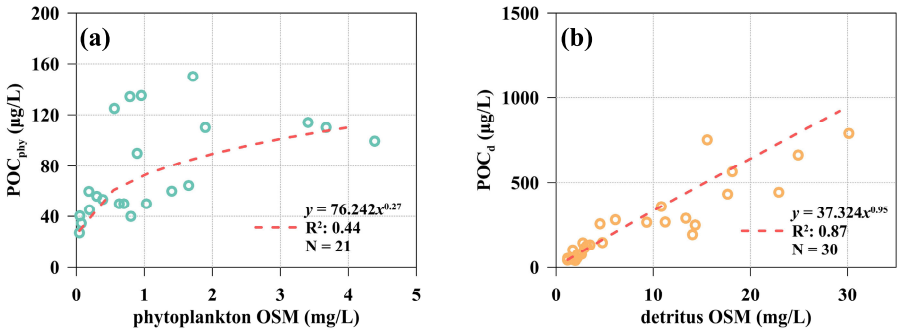

Fig. 10. Relationship between (a) phytoplankton-dominated samples OSM concentration and POC and (b) detritus-dominated samples OSM concentration and POC. The dotted red line indicates the fit curve. The dominated particle type is determined by $Q_{bbe}(682)$ in this section.

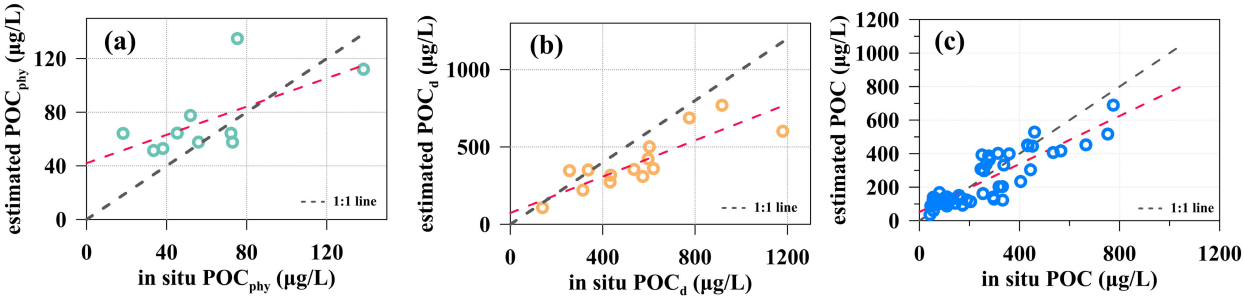

Fig. 11. Comparison between each component of POC contribution and total POC estimation in this study and in situ POC measurements (a) POC_{phy}, (b) POD_d, and (c) total POC. The dashed gray lines represent the 1:1 line.

IV. Results

A. Validation for R_{rs}, OSM, and TSM

R_{rs}, OSM, and TSM results obtained from OLCI images after C2RCC atmospheric correction are validated using in situ data during the 2020 cruises. We selected satellite images taken within 3 h before and after the sampling time at each station. Using the sampling point as the center, we calculated the spatial average of a 3 × 3 pixel area to obtain the R_{rs} detected by the satellite at that station. The ten matchup stations between the Sentinel-3/OLCI overpasses and in situ data were used for the validation of the OLCI R_{rs}, TSM, and OSM. The validation results are shown in Fig. 12.

Fig. 12(a) and (b) show the comparations of Sentinel-3/OLCI atmospheric-corrected R_{rs} of 665 and 682 nm with in situ measurements. Overall, the applicability of the C2RCC atmospheric correction algorithm in optically complex environments is good ($N = 47$, $p < 0.05$), with points distributed along the 1:1 line. For the 665 nm, the RMSE is 0.0018 sr^{-1}, and the MAPE is 48.91%. For the 682 nm, the RMSE is 0.0018 sr^{-1}, and the MAPE is 50.67%.

A comparison of the retrieved OSM from Sentinel 3/OLCI to the in situ OSM is reported in Fig. 12(c) ($N = 11$, $p < 0.05$) and shows RMSE of 6.88% and MAPE of 21.85%. As for the SERT validation, the results are shown in Fig. 12(d) ($N = 14$, $p < 0.05$). The RMSE is 0.0025 g L^{-1}, with a MAPE of 34.54%. The result demonstrates the improved-coefficient SERT developed in this study gave good TSM estimates in the study area; therefore, in spite of the lack of POC in situ data collection in 2020, the validation based on atmospheric correction results, in situ R_{rs}, TSM, and OSM data confirms the applicability of the algorithm developed in this study.

B. Sentinel-3/OLCI-Derived POC_{phy}, POC_d, and Total POC

Sentinel-3/OLCI for the entire year of 2020 was processed, and monthly average POC_{phy}, POC_d, and total POC were calculated, as shown in Figs. 13–15. It should be noted that due to high cloud cover in the data for January and December

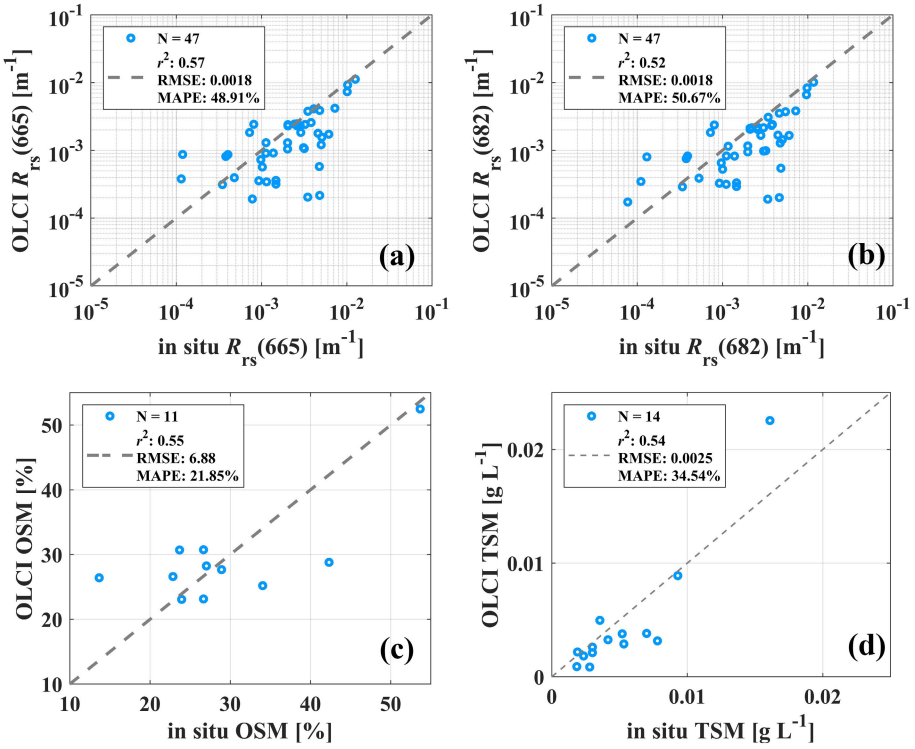

Fig. 12. Match-up comparisons of (a) $R_{rs}(665)$, (b) $R_{rs}(682)$, (c) OSM, and (d) TSM obtained from Sentinel-3/OLCI and in situ measurements. The dashed gray line represents the 1:1 line.

2020, the monthly average products still contain significant blanks. Because of the significant sun glint in the southeast part of the East China Sea, the data quality from Sentinel-3/OLCI imaging in that area cannot be guaranteed. As a result, POC values in this region should be regarded with suspicion.

Fig. 13 shows Sentinel-3/OLCI POC_{phy} retrieved from January to December 2020. Overall, noticeable seasonal and spatial differences were observed in POC_{phy}. In general, POC_{phy} remained below 50 μg L^{-1} at the mouth of estuaries, estuarine TMZ, and Subei Shoal throughout the year; however, there were significant seasonal variations at the estuarine particle front. During winter (DJF), POC_{phy} values generally remained lower than in spring and summer (below 80 μg L^{-1}). In spring (MAM), POC_{phy} was primarily concentrated in the central BS and along the coastal particle front, with the highest levels in May reaching around 200 μg L^{-1} at the particle front outside YRE and in the central BS, then it gradually decreased in the summer and autumn. Fig. 14 illustrates Sentinel-3/OLCI POC_d retrieved from January to December 2020. It is observed that there were POC_d also significant seasonal-spatial distribution variations. Primarily, in the areas around the Yangtze River, the Yellow River, the Liaohe River, and the Yalu River estuaries, inside of their TMZ, the Hangzhou Bay, and the Subei Shoal, POC_d values maintain high levels throughout the year (greater than 100 μg L^{-1}), with the highest levels found within the Subei Shoal and Hangzhou Bay, consistently exceeding 800 μg L^{-1}. Additionally, during the winter and early spring, high POC_d values are widespread in the central BS and at the particle plume outside the YRE. In contrast, during the summer, the high POC_d area is less, increasing gradually in the autumn; therefore, by adding the distributions of POC_{phy} and POC_d, the total POC values were obtained, as shown in Fig. 15. It is shown that in the total POC, POC_d made the primary contribution in estuarine and nearshore areas, while outside the estuaries, POC_{phy} constitutes the major component.

V. Discussions

A. Particle Compositions Discrimination

The estuarine-coastal-shelf sea regions connect the carbon cycle between continents and oceans and also lead to relatively active carbon cycling. POC sources in this region are complex, from rivers delivering large amounts of terrestrial particles to oceanic phytoplankton production and cycling [60], [61]. Distinguishing and identifying the contributions of detrital particles and phytoplankton from estuaries is vital for estimating the carbon sequestration capacity and the global carbon contribution of coastal and estuarine waters [62], [63].

Remote sensing-based estimates of POC in open waters have achieved a relatively well-established accuracy range accepted by the community [1], [64]. In open ocean areas, variability in the inherent optical properties of particles is primarily driven by a mixture of phytoplankton and covarying detritus, which are the major contributors to POC. In the estuarine-coastal-shelf waters, POC sources vary from marine, estuaries, riverine, etc., including contributions from phytoplankton and organic detritus [65], [66]. These multiple sources not only contribute to different POC components but also result in an extremely complex combination of the optical

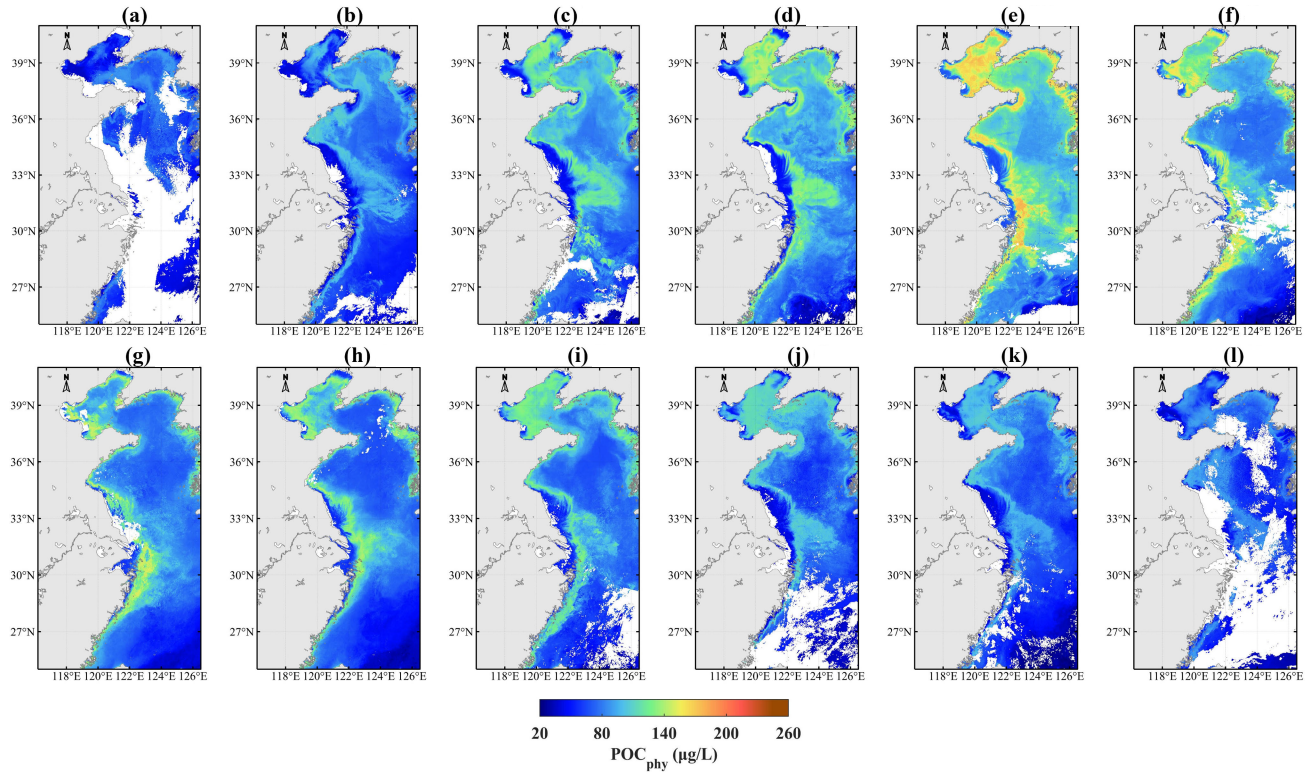

Fig. 13. 2020 monthly averaged Sentinel-3/OLCI POC_{phy} images in the Eastern Seas of China. (a) January. (b) February. (c) March. (d) April. (e) May. (f) June. (g) July. (h) August. (i) September. (j) October. (k) November. (l) December.

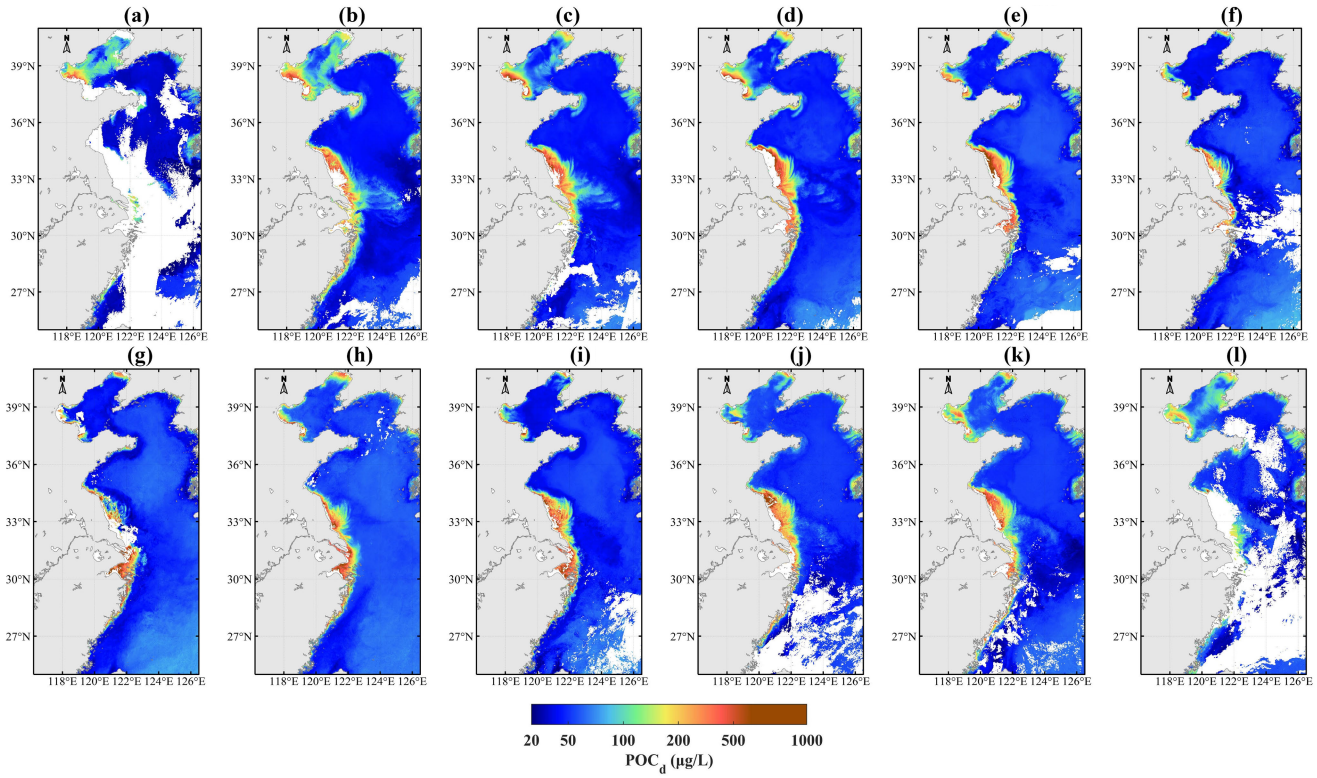

Fig. 14. 2020 monthly averaged Sentinel-3/OLCI POC_d images in the Eastern Seas of China. (a) January. (b) February. (c) March. (d) April. (e) May. (f) June. (g) July. (h) August. (i) September. (j) October. (k) November. (l) December.

environments [52], [67], [68]. This poses challenges in applying individual proxies for POC inversion in estuarine-coastal environments characterized by diverse optical conditions and particle compositions [12], [15].

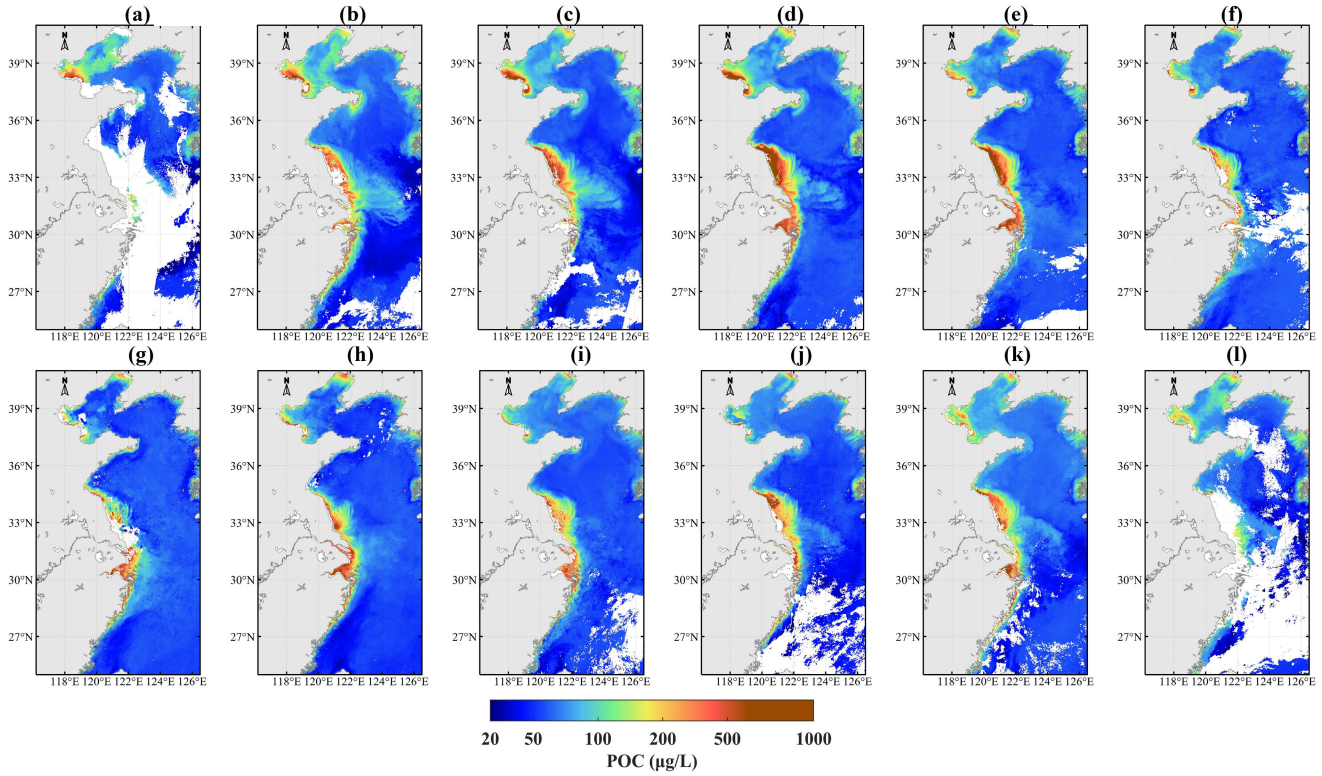

Fig. 15. 2020 monthly averaged Sentinel-3/OLCI total POC images in the Eastern Seas of China. (a) January. (b) February. (c) March. (d) April. (e) May. (f) June. (g) July. (h) August. (i) September. (j) October. (k) November. (l) December.

To distinguish different particle contributions to POC and calculate total POC in the highly complex optical environment of these waters, we have developed a categorized POC estimation method based on particle compositions. This algorithm not only enhances the accuracy of POC estimation but also provides a separation of POC contributions of phytoplankton and organic detritus. Then, the algorithm was applied to Sentinel-3/OLCI data in 2020; the calculation of monthly POC_{phy}, POC_{d}, and total POC reveals significant spatiotemporal variations, contributing to a better understanding of the carbon pool in the optically complex waters of the estuarine-coastal-shelf sea waters.

Here, the algorithm proposed in this study, together with widely employed POC inversion algorithms, were applied to in situ $R_{rs}(\lambda)$ and compared with in situ POC measurements (Fig. 16, Table IV). The blue-green ratio algorithm ($Stramski08_{recal}$ [16], in Fig. 16) exhibits significant biases in estimating POC in coastal waters, with a notable underestimation of high POC samples, yielding R^2 of 0.34, RMSE of 88.51 μg L^{-1}, and MAPE of 51.39% ($N = 60$). This is possibly due to the saturation of the blue and green band of R_{rs}, particularly in highly turbid waters such as estuaries and nearshore regions [69], which can lead to a severe underestimation of POC. For the multivariate regression method ($Le17_{recal}$ [17], in Fig. 16), the points are generally clustered around the 1:1 line. Overall, R^2 is higher than that of $Stramski08_{recal}$, at 0.45. The performance of this algorithm in POC-rich waters (>200 μg L^{-1}) is closer to the 1:1 line when compared to Wei19 and $Stramski08_{recal}$, while in low POC regions, there exhibits a noticeable underestimation. The water-classification-based algorithm (Wei19 [13], in Fig. 16) is generally more suitable for turbid and complex waters compared to $Le17_{recal}$ and $Stramski08_{recal}$, with an R^2 of 0.67 and MAPE of 53.95%. The overall underestimations of Chl*a*, which is selected as the proxy of the low-TSM waters, lead to underestimations on the POC in low-TSM samples.

TABLE IV

ACCURACY STATISTICS OF THE DIFFERENT POC MODELS (IN THIS STUDY, WEI ET AL. [13], LE ET AL. [17], AND STRAMSKI ET AL. [16]). BASED ON THE INDEPENDENT VALIDATION DATASET. THE NUMBER OF VALID IN SITU POC DATA IS 60

	This study	Wei19	$Le17_{recal}$	$Stramski08_{recal}$
RMSE [μg L^{-1}]	16.57	23.91	22.55	88.51
MAPE	43.97%	53.95%	52.20%	51.39%
R^2	0.71	0.67	0.45	0.34

The algorithm developed in this study exhibited reasonable performance, with an R^2 value of 0.71, MAPE of 43.97%, and RMSE of 16.57 μg L^{-1}. It is observed that this method tends to show relative overestimation in cases with low POC levels. On one hand, this is due to some underestimation in fitting lower POC_{phy} content during the establishment from phytoplankton OSM [Fig. 10(a)]. Further optimization of coefficients and models is required, which can be achieved by accumulating station data on phytoplankton-driven POC in upcoming in situ observation plans. On the other hand,

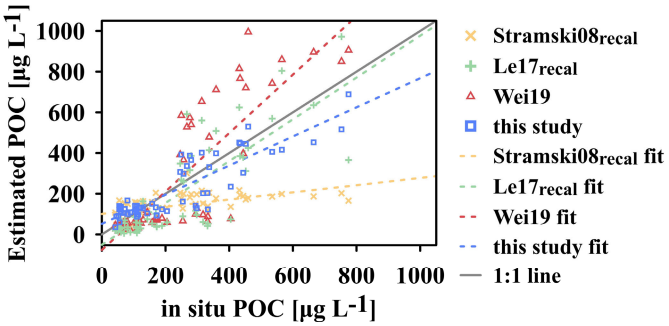

Fig. 16. Comparison between the POC algorithms (by Stramski et al. [16], Le et al. [17], Wei et al. [13], and this study) and in situ POC measurements. The yellow multiplication, green crosses, red triangle, and blue squares represent the POC derived from Stramski08$_{recal}$, Le17$_{recal}$, Wei19, and this study, respectively. The dotted gray lines represent the 1:1 line.

combining Figs. 9(b) and 12(c) reveal that there is underestimation in areas with low OSM. In waters with relatively high levels of mineral particles, the underestimation of OSM, therefore, results in the underestimation of POC. Another factor is the assumption for the dominant particle types during the development of POC and OSM, which may lead to potentially incomplete separation of dominant particles. While such assumptions and optical classifications are necessary in this study, reasonable methods should be applied to collect in situ data of phytoplankton carbon and organic detritus carbon for the optimization of optical classification models in further plans. This could include applying empirical relationships that relate cell biovolume to phytoplankton carbon [70], [71], separating living particles with flow-cytometric analysis [72], [73], and employing ^{14}C labeling cultivation [74]. Meanwhile, the relationship between γ and OSM established is empirical (see Fig. 9). It is worth noting that, theoretically, particle size will also have an impact on γ. Although Q_{bbe} was used to minimize the influence of particle size in establishing the POC contribution of each particle component, the in situ measurements of Chl*a*, particle size distribution (PSD), and OSM in 2020 are provided in Supplement document Fig. S5 for readers' reference. In this study, in situ data was used to verify Sentinel-3/OLCI R_{rs}, TSM, and OSM. Because of the lack of synchronous in situ POC data for the year 2020, the comparison of satellite POC inversion results is lacking; thus, it is necessary to collect the in situ POC data in the following research plans and compare it with the satellite results.

Because the dataset used in primarily establishing this model pertains to complex optical environments in estuarine, coastal, and shelf seas, as well as the empirical analysis of particle compositions and the selection of the red spectral band, the applicability of this work to open ocean oligotrophic waters will need to be assessed through in situ data collection and analysis. Nevertheless, this work emphasizes the need for compositional analysis in complex waters due to the improved understanding of the relationship between particle composition and optical properties, as well as the wide range of variability in particle characteristics and optical properties. In this study, the POC inversion based on the classification of particle types can fundamentally separate the POC contributions of different particles and also analyze the content of different particle compositions and their contribution to POC. This approach has the potential to be extended to global estuarine-coastal-shelf sea waters characterized by turbid conditions and complex particle compositions, thus offering a novel perspective for analyzing POC contributions and conducting carbon pool research.

B. Spatial Distribution of POC in Estuarine-Coastal-Shelf Waters

In this section, the focus is on the spatiotemporal distribution of POC$_{phy}$, POC$_d$ contributions, as well as total POC by integrating the results with previous research. Spatiotemporal distributions of POC$_{phy}$ and POC$_d$ in 2020 are shown in Figs. 13 and 14.

In terms of spatial distribution, within the estuarine particle front, particle flocculation weakens while salinity increases from the estuary toward offshore, resulting in reduced light-blocking effects, and these waters are rich in nutrients, leading to higher POC$_{phy}$ levels in the spring, which can even trigger algal blooms [75], [76], [77]. As moving seaward, nutrient levels decrease and seawater salinity increases, leading to a decrease in phytoplankton biomass that eventually stabilizes [78]; however, in the estuaries of large rivers, within their TMZ, and in the Subei Shoal, the high turbidity waters inhibit the growth of phytoplankton. Consequently, POC$_{phy}$ in this region is lower than that in the estuarine particle front, with a significant POC contribution from organic detritus [76], [77], [79].

Regarding temporal distribution, during autumn (SON) and winter (DJF), terrestrial organic detritus has a significant POC contribution to the BS and nearshore waters, primarily due to anthropogenic factors and the inflow of terrestrial organic particles from the Yellow River [80], [81]. In spring (MAM) and summer (JJA), the phytoplankton-typed POC from the central Yellow-BS and offshore waters gradually increase, becoming dominant [63], [80].

In summary, the results are consistent with previous in situ research; furthermore, beyond the algorithmic improvements in total POC retrieval compared to earlier research, these results have the potential to be applied to long-term satellite remote sensing data for assessing the spatiotemporal distribution of POC contributions from different particle components in estuarine-coastal-shelf sea waters. This holds significant potential for investigating the dynamic changes in coastal particle composition and variations in local carbon pools.

VI. Conclusion

Understanding the contributions of different types and sources of particles to the nearshore area is crucial for comprehending the estuarine-coastal-shelf sea carbon cycle. To achieve this, we proposed differentiating between organic detritus and phytoplankton and estimating their contributions to POC using optical properties. An extensive in situ dataset representing various particle compositions and optical properties was collected, including data from highly turbid estuarine water and shelf seawater. QAA algorithm for nearshore turbid

TABLE V
MAIN PARAMETERS USED IN THIS STUDY AND THEIR BRIEF DESCRIPTIONS

Main parameters and notations	Description	Unit
$a_x(\lambda)$	Absorption coefficient, where x = n_w, p, ph, NAP, g, and dg specifies total non-water, particulate, phytoplankton, non-algal particle, Chromophoric Dissolved Organic Matter (CDOM), and CDOM with non-algal particle, respectively	m^{-1}
$b_{bp}(\lambda)$	Particulate backscattering coefficient	m^{-1}
Chl$a$	Chlorophyll a concentration	$\mu g\ L^{-1}$
$E_d(\lambda)$	Downwelling irradiance just above the sea surface,	$W\ m^{-2}\ nm^{-1}$
$L_x(\lambda)$	Spectral radiance, where x = tot, and s,sky specifies total, and sky incoming spectral radiance, respectively	$W\ m^{-2}\ sr^{-1}\ nm^{-1}$
OSM	Organic suspended matter mass fraction,	%
POC	Total particulate organic carbon,	$\mu g\ L^{-1}$
POC_x	Particulate organic carbon, where x = phy, and d specifies phytoplankton, and organic detritus, respectively,	$\mu g\ L^{-1}$
Q_{bbe}	Particulate backscattering efficiency factors	dimensionless
$R_{rs}(\lambda)$	Above-surface remote-sensing reflectance	sr^{-1}
$r_{rs}(\lambda)$	Below-surface remote-sensing reflectance	sr^{-1}
S_{dg}	Spectral slope for $a_{dg}(\lambda)$	nm^{-1}
TSM	Total suspended particulate matter	$g\ L^{-1}$
$\beta_x(\lambda,\theta)$	Volume scattering function, where x = t, and w specifies total and water, respectively,	$sr^{-1}\ m^{-1}$
γ	Spectral slope of $b_{bp}(\lambda)$	dimensionless
$\rho_{sky}(\lambda)$	Sky radiance spectral reflectance	dimensionless
$\chi_p(\lambda)$	Conversion coefficient from $\beta(\lambda,\theta)$ to $b_{bp}(\lambda)$	dimensionless

waters was fined-tuned to calculate the particulate inherent optical properties based on $R_{rs}(\lambda)$, including the $b_{bp}(\lambda)$ with its spectral slope and $a_{ph}(\lambda)$ and $a_{NAP}(\lambda)$. The tuned QAA algorithm was validated using independent in situ data, and it showed improved calculations for $b_{bp}(682)$ and $a_{ph}(\lambda)/a_{NAP}(\lambda)$, with R^2 values of 0.88 and 0.44, respectively. In addition, the SERT algorithm was recalibrated using the extensive in situ data to estimate TSM, with an R^2 of 0.91.

We developed the relationship between the OSM mass proportion and $b_{bp}(\lambda)$ slope γ obtained by QAA ($R^2 = 0.81$), to obtain OSM mass proportion. Then, POC_d and POC_{phy} were estimated according to $a_{ph}(\lambda)/a_{NAP}(\lambda)$ and OSM. It is indicated that the proposed algorithm is effective and promising in quantitatively classifying particle composition and accurately estimating the POC contributions with in situ $R_{rs}(\lambda)$, with R^2 and RMSE values of 0.71 and 16.57 $\mu g\ L^{-1}$, respectively. This encourages the application of the algorithm to Sentinel-3/OLCI estimating POC_d and POC_{phy}, OSM, and finally assessing seasonal and spatial variability from space. The comparison between remote sensing inversion and in situ station distribution results revealed consistent spatial patterns.

ACKNOWLEDGMENT

The authors would like to express our sincere appreciation to the two anonymous reviewers and the editor for their valuable and constructive input in enhancing the quality of our work. *Author Contributions:* Fang Shen provided project administration. Fang Shen and Mengyu Li conceptualized and designed the study. Mengyu Li processed data and prepared and figures, tables. Mengyu Li, Fang Shen, and Emanuele Organelli contributed to writing and revising the manuscript. Mengyu Li and Wei Luo conducted field data sampling and laboratory analyses. Renhu Li processed Sentinel-3/OLCI data. Xuerong Sun analyzed absorption data. Xiaodao Wei prepared historical data. All authors provided feedback and approved the final version. The historical optical and biogeochemical data from 2014 to 2015 are available at Wei et al. [13] via http://doi.org/10.1029/2018jc014715. New dataset, figures are available at http://doi.org/10.6084/m9.figshare.22822676. Coastline data can be obtained from https://www.soest.hawaii.edu/pwessel/gshhg, bathymetry maps dataset can be download from https://www.ngdc.noaa.gov/mgg/global/relief/ETOPO1.

APPENDIX

The main parameters used in this study and their brief descriptions are shown in Table V.

REFERENCES

[1] R. J. W. Brewin et al., "Sensing the ocean biological carbon pump from space: A review of capabilities, concepts, research gaps and future developments," *Earth-Sci. Rev.*, vol. 217, Jun. 2021, Art. no. 103604, doi: 10.1016/j.earscirev.2021.103604.

[2] D. Stramski, E. Boss, D. Bogucki, and K. J. Voss, "The role of seawater constituents in light backscattering in the ocean," *Prog. Oceanogr.*, vol. 61, no. 1, pp. 27–56, Apr. 2004, doi: 10.1016/j.pocean.2004.07.001.

[3] D. W. Menzel and J. J. Goering, "The distribution of organic detritus in the ocean," *Limnology Oceanogr.*, vol. 11, no. 3, pp. 333–337, Apr. 1966, doi: 10.4319/lo.1966.11.3.0333.

[4] K. Bisson, D. A. Siegel, and T. DeVries, "Diagnosing mechanisms of ocean carbon export in a satellite-based food web model," *Frontiers Mar. Sci.*, vol. 7, p. 505, Jul. 2020, doi: 10.3389/fmars.2020.00505.

[5] A.-S. Heiskanen, and A. Keck, "Distribution and sinking rates of phytoplankton, detritus, and particulate biogenic silica in the Laptev Sea and Lena River (Arctic Siberia)," *Mar. Chem.*, vol. 53, nos. 3–4, pp. 229–245, 1996, doi: 10.1016/0304-4203(95)00091-7.

[6] R. J. W. Brewin et al., "Ocean carbon from space: Current status and priorities for the next decade," *Earth-Sci. Rev.*, vol. 240, May 2023, Art. no. 104386, doi: 10.1016/j.earscirev.2023.104386.

[7] X. Sun, F. Shen, D. Liu, R. G. J. Bellerby, Y. Liu, and R. Tang, "In situ and satellite observations of phytoplankton size classes in the entire continental shelf sea, China," *J. Geophys. Res., Oceans*, vol. 123, no. 5, pp. 3523–3544, May 2018, doi: 10.1029/2017jc013651.

[8] W. Luo, F. Shen, Q. He, F. Cao, H. Zhao, and M. Li, "Changes in suspended sediments in the Yangtze river estuary from 1984 to 2020: Responses to basin and estuarine engineering constructions," *Sci. Total Environ.*, vol. 805, Jan. 2022, Art. no. 150381, doi: 10.1016/j.scitotenv.2021.150381.

[9] F. Shen, W. Verhoef, Y. Zhou, M. S. Salama, and X. Liu, "Satellite estimates of wide-range suspended sediment concentrations in Changjiang (Yangtze) estuary using MERIS data," *Estuaries Coasts*, vol. 33, no. 6, pp. 1420–1429, Nov. 2010, doi: 10.1007/s12237-010-9313-2.

[10] D. Pan, Q. Liu, and Y. Bai, "Review and suggestions for estimating particulate organic carbon and dissolved organic carbon inventories in the ocean using remote sensing data," *Acta Oceanolog. Sinica*, vol. 33, no. 1, pp. 1–10, Jan. 2014, doi: 10.1007/s13131-014-0419-4.

[11] R. A. Reynolds, D. Stramski, V. M. Wright, and S. B. Woźniak, "Measurements and characterization of particle size distributions in coastal waters," *J. Geophys. Res., Oceans*, vol. 115, no. C8, Aug. 2010, Art. no. C08024, doi: 10.1029/2009jc005930.

[12] T. K. Tran et al., "Deriving particulate organic carbon in coastal waters from remote sensing: Inter-comparison exercise and development of a maximum band-ratio approach," *Remote Sens.*, vol. 11, no. 23, p. 2849, Nov. 2019, doi: 10.3390/rs11232849.

[13] X. Wei, F. Shen, Y. Pan, S. Chen, X. Sun, and Y. Wang, "Satellite observations of the diurnal dynamics of particulate organic carbon in optically complex coastal oceans: The continental shelf seas of China," *J. Geophys. Res., Oceans*, vol. 124, no. 7, pp. 4710–4726, Jul. 2019, doi: 10.1029/2018jc014715.

[14] Y. Wang, F. Shen, L. Sokoletsky, and X. Sun, "Validation and calibration of QAA algorithm for CDOM absorption retrieval in the Changjiang (Yangtze) estuarine and coastal waters," *Remote Sens.*, vol. 9, no. 11, p. 1192, Nov. 2017, doi: 10.3390/rs9111192.

[15] D. Stramski, S. Constantin, and R. A. Reynolds, "Adaptive optical algorithms with differentiation of water bodies based on varying composition of suspended particulate matter: A case study for estimating the particulate organic carbon concentration in the Western Arctic seas," *Remote Sens. Environ.*, vol. 286, Mar. 2023, Art. no. 113360, doi: 10.1016/j.rse.2022.113360.

[16] D. Stramski et al., "Relationships between the surface concentration of particulate organic carbon and optical properties in the eastern South Pacific and eastern Atlantic Oceans," *Biogeosciences*, vol. 5, no. 1, pp. 171–201, Feb. 2008, doi: 10.5194/bg-5-171-2008.

[17] C. Le, J. C. Lehrter, C. Hu, H. MacIntyre, and M. W. Beck, "Satellite observation of particulate organic carbon dynamics on the Louisiana continental shelf," *J. Geophys. Res., Oceans*, vol. 122, no. 1, pp. 555–569, Jan. 2017, doi: 10.1002/2016JC012275.

[18] C. Le, X. Zhou, C. Hu, Z. Lee, L. Li, and D. Stramski, "A color-index-based empirical algorithm for determining particulate organic carbon concentration in the ocean from satellite observations," *J. Geophys. Res., Oceans*, vol. 123, no. 10, pp. 7407–7419, Oct. 2018, doi: 10.1029/2018JC014014.

[19] A. N. Tyler, P. D. Hunter, E. Spyrakos, S. Groom, A. M. Constantinescu, and J. Kitchen, "Developments in Earth observation for the assessment and monitoring of inland, transitional, coastal and shelf-sea waters," *Sci. Total Environ.*, vol. 572, pp. 1307–1321, Dec. 2016, doi: 10.1016/j.scitotenv.2016.01.020.

[20] Z. Lee, K. L. Carder, and R. A. Arnone, "Deriving inherent optical properties from water color: A multiband quasi-analytical algorithm for optically deep waters," *Appl. Opt.*, vol. 41, no. 27, p. 5755, Sep. 2002, doi: 10.1364/AO.41.005755.

[21] F. Shen, Y. Zhou, J. Li, Q. He, and W. Verhoef, "Remotely sensed variability of the suspended sediment concentration and its response to decreased river discharge in the Yangtze estuary and adjacent coast," *Continental Shelf Res.*, vol. 69, pp. 52–61, Oct. 2013, doi: 10.1016/j.csr.2013.09.002.

[22] J. Mueller, R. Bidigare, and C. Trees, *Biogeochemical and Bio-Optical Measurements and Data Analysis Protocols: Ocean Optics Protocols for Satellite Ocean Color Sensor Validation, Revision 4*, document NASA/TM-2003 21621, 2003.

[23] J. D. H. Strickland and T. R. Parsons, *A Practical Handbook of Seawater Analysis*, 2nd ed. Ottawa, ON, Canada: Fisheries Research Board of Canada, 1972, p. 310.

[24] S. Pegau, J. R. V. Zaneveld, and B. G. Mitchell, "Inherent optical properties: Instruments, characterization, field measurements and data analysis protocols," in *Ocean Optics Protocols for Satellite Ocean Color Sensor Validation, Revision 4*, vol. 4, J. L. Mueller, G. S. Fargion and C. R. McClain, Eds. Greenbelt, MD, USA: National Aeronautical and Space Administration, Goddard Space Flight Space Center, 2003, p. 76.

[25] C. Roesler, D. Stramski, and E. D'Sa, "Spectrophotometric measurements of particulate absorption using filter pads," in *IOCCG Protocol Series Ocean Optics & Biogeochemistry Protocols for Satellite Ocean Colour Sensor Validation, Inherent Optical Property Measurements and Protocols: Absorption Coefficient (v1.0)*, vol. 1, A. R. Neeley and A. Mannino, Eds. Dartmouth, NS, Canada: International Ocean Colour Coordinating Group (IOCCG) in Collaboration withNational Aeronautics and Space Administration (NASA), 2018.

[26] R. Röttgers and S. Gehnke, "Measurement of light absorption by aquatic particles: Improvement of the quantitative filter technique by use of an integrating sphere approach," *Appl. Opt.*, vol. 51, no. 9, p. 1336, 2012, doi: 10.1364/AO.51.001336.

[27] W. S. Pegau et al., "A comparison of methods for the measurement of the absorption coefficient in natural waters," *J. Geophys. Res., Oceans*, vol. 100, no. C7, pp. 13201–13220, Jul. 1995, doi: 10.1029/95JC00456.

[28] J. L. Mueller, G. S. Fargion, and C. R. McClain, *Ocean Optics Protocols for Satellite Ocean Color Sensor Validation, Revision 4, Inherent Optical Properties: Instruments, Characterizations, Field Measurements and Data Analysis Protocols*. Greenbelt, MD, USA: Goddard Space Flight Space Center, 2003.

[29] WETLabs. (2023). *Scattering Meter BB9 User's Guide*. [Online]. Available: https://www.comm-tec.com/prods/mfgs/Wetlabs/Manuals/Eco-BB9_manual.pdf

[30] E. Boss and W. S. Pegau, "Relationship of light scattering at an angle in the backward direction to the backscattering coefficient," *Appl. Opt.*, vol. 40, no. 30, p. 5503, Oct. 2001, doi: 10.1364/AO.40.005503.

[31] T. Oishi, "Significant relationship between the backward scattering coefficient of sea water and the scatterance at 120°," *Appl. Opt.*, vol. 29, no. 31, p. 4658, 1990, doi: 10.1364/AO.29.004658.

[32] R. A. Maffione and D. R. Dana, "Instruments and methods for measuring the backward-scattering coefficient of ocean waters," *Appl. Opt.*, vol. 36, no. 24, p. 6057, Aug. 1997, doi: 10.1364/ao.36.006057.

[33] X. Zhang, L. Hu, and M.-X. He, "Scattering by pure seawater: Effect of salinity," *Opt. Exp.*, vol. 17, no. 7, p. 5698, Mar. 2009, doi: 10.1364/oe.17.005698.

[34] X. Zhang and L. Hu, "Estimating scattering of pure water from density fluctuation of the refractive index," *Opt. Exp.*, vol. 17, no. 3, p. 1671, Feb. 2009, doi: 10.1364/oe.17.001671.

[35] J. M. Sullivan, M. S. Twardowski, and J. Ronald, "Measuring optical backscattering in water," in *Light Scattering Reviews*, vol. 7. Berlin, Germany: Springer, 2013, pp. 189–224.

[36] Z. Lee, Y.-H. Ahn, C. Mobley, and R. Arnone, "Removal of surface-reflected light for the measurement of remote-sensing reflectance from an above-surface platform," *Opt. Exp.*, vol. 18, no. 25, p. 26313, 2010, doi: 10.1364/OE.18.026313.

[37] F. Shen, Y. Zhou, X. Peng, and Y. Chen, "Satellite multi-sensor mapping of suspended particulate matter in turbid estuarine and coastal ocean, China," *Int. J. Remote Sens.*, vol. 35, nos. 11–12, pp. 4173–4192, Jun. 2014, doi: 10.1080/01431161.2014.916053.

[38] L. G. Sokoletsky and F. Shen, "Optical closure for remote-sensing reflectance based on accurate radiative transfer approximations: The case of the Changjiang (Yangtze) river estuary and its adjacent coastal area, China," *Int. J. Remote Sens.*, vol. 35, nos. 11–12, pp. 4193–4224, Jun. 2014, doi: 10.1080/01431161.2014.916048.

[39] G. Neukermans, K. Ruddick, H. Loisel, and P. Roose, "Optimization and quality control of suspended particulate matter concentration measurement using turbidity measurements," *Limnol. Oceanogr., Methods*, vol. 10, no. 12, pp. 1011–1023, Dec. 2012, doi: 10.4319/lom.2012.10.1011.

[40] M. Schartau et al., "On the separation between inorganic and organic fractions of suspended matter in a marine coastal environment," *Prog. Oceanogr.*, vol. 171, pp. 231–250, Feb. 2019, doi: 10.1016/j.pocean.2018.12.011.

[41] D. Sun et al., "Light scattering properties and their relation to the biogeochemical composition of turbid productive waters: A case study of lake Taihu," *Appl. Opt.*, vol. 48, no. 11, p. 1979, 2009, doi: 10.1364/AO.48.001979.

[42] Sequoia-Scientific. (Dec. 28, 2020). *LISST-200X User's Manual Version 2.1*. [Online]. Available: https://www.sequoiasci.com/wp-content/uploads/2016/02/LISST-200X-Users-Manual-v2_1.pdf

[43] A. Knap, A. Michaels, and A. Close, *Protocols for the Joint Global Ocean Flux Study (JGOFS) Core Measurements*, vol. 19. Paris, France: UNESCO-IOC, 1996.

[44] J. I. Hedges and J. H. Stern, "Carbon and nitrogen determinations of carbonate-containing solids1," *Limnol. Oceanogr.*, vol. 29, no. 3, pp. 657–663, May 1984, doi: 10.4319/lo.1984.29.3.0657.

[45] R. Doerffer and H. Schiller, "The MERIS case 2 water algorithm," *Int. J. Remote Sens.*, vol. 28, nos. 3–4, pp. 517–535, Feb. 2007, doi: 10.1080/01431160600821127.

[46] H. Zhao, F. Shen, and X. Sun, "Remote sensing retrieval of phytoplankton group in the eastern China seas," *Acta Oceanolog. Sin.*, vol. 4, no. 22, pp. 153–168, 2022, doi: 10.12284/hyxb2022062.

[47] W. Yang, B. Matsushita, J. Chen, K. Yoshimura, and T. Fukushima, "Retrieval of inherent optical properties for turbid inland waters from remote-sensing reflectance," *IEEE Trans. Geosci. Remote Sens.*, vol. 51, no. 6, pp. 3761–3773, Jun. 2013, doi: 10.1109/TGRS.2012.2220147.

[48] W. Wang, Q. Dong, and S. Shang, "An evaluation of two semi-analytical ocean color algorithms for waters of the South China Sea," *J. Trop. Oceanogr.*, vol. 28, no. 5, pp. 35–42, 2009, doi: 10.11978/j.issn.1009-5470.2009.05.035.

[49] S. Lei et al., "A semi-analytical algorithm for deriving the particle size distribution slope of turbid inland water based on OLCI data: A case study in lake Hongze," *Environ. Pollut.*, vol. 270, Feb. 2021, Art. no. 116288, doi: 10.1016/j.envpol.2020.116288.

[50] A. Morel, "Optics of marine particles and marine optics," in *Particle Analysis in Oceanography*. Cham, Switzerland: Springer, 1991, pp. 141–188.

[51] R. A. Reynolds, D. Stramski, and G. Neukermans, "Optical backscattering by particles in Arctic seawater and relationships to particle mass concentration, size distribution, and bulk composition," *Limnology Oceanogr.*, vol. 61, no. 5, pp. 1869–1890, Sep. 2016, doi: 10.1002/lno.10341.

[52] M. S. Twardowski, E. Boss, J. B. Macdonald, W. S. Pegau, A. H. Barnard, and J. R. V. Zaneveld, "A model for estimating bulk refractive index from the optical backscattering ratio and the implications for understanding particle composition in case I and case II waters," *J. Geophys. Res., Oceans*, vol. 106, no. C7, pp. 14129–14142, Jul. 2001, doi: 10.1029/2000jc000404.

[53] S. B. Woźniak et al., "Optical variability of seawater in relation to particle concentration, composition, and size distribution in the nearshore marine environment at imperial beach, California," *J. Geophys. Res., Oceans*, vol. 115, no. C8, Aug. 2010, Art. no. C08027, doi: 10.1029/2009JC005554.

[54] D. G. Bowers, P. S. Hill, and K. M. Braithwaite, "The effect of particulate organic content on the remote sensing of marine suspended sediments," *Remote Sens. Environ.*, vol. 144, pp. 172–178, Mar. 2014, doi: 10.1016/j.rse.2014.01.005.

[55] R. D. Vaillancourt, "Light backscattering properties of marine phytoplankton: Relationships to cell size, chemical composition and taxonomy," *J. Plankton Res.*, vol. 26, no. 2, pp. 191–212, Feb. 2004, doi: 10.1093/plankt/fbh012.

[56] A. L. Whitmire, W. S. Pegau, L. Karp-Boss, E. Boss, and T. J. Cowles, "Spectral backscattering properties of marine phytoplankton cultures," *Opt. Exp.*, vol. 18, no. 14, p. 15073, Jul. 2010, doi: 10.1364/OE.18.015073.

[57] S. Wang et al., "Variability in the backscattering efficiency of particles in the Bohai and yellow seas and related effects on optical properties," *Opt. Exp.*, vol. 24, no. 26, p. 29360, 2016, doi: 10.1364/OE.24.029360.

[58] D. G. Bowers and K. M. Braithwaite, "Evidence that satellites sense the cross-sectional area of suspended particles in shelf seas and estuaries better than their mass," *Geo-Marine Lett.*, vol. 32, no. 2, pp. 165–171, Apr. 2012, doi: 10.1007/s00367-011-0259-6.

[59] S. Wang et al., "Remote sensing of particle cross-sectional area in the Bohai sea and yellow sea: Algorithm development and application implications," *Remote Sens.*, vol. 8, no. 10, p. 841, Oct. 2016, doi: 10.3390/rs8100841.

[60] P. A. Raymond and J. E. Bauer, "Use of 14C and 13C natural abundances for evaluating riverine, estuarine, and coastal DOC and POC sources and cycling: A review and synthesis," *Org. Geochem.*, vol. 32, no. 4, pp. 469–485, 2001, doi: 10.1016/S0146-6380(00)00190-X.

[61] X.-C. Wang, R. F. Chen, and G. B. Gardner, "Sources and transport of dissolved and particulate organic carbon in the Mississippi river estuary and adjacent coastal waters of the northern Gulf of Mexico," *Mar. Chem.*, vol. 89, nos. 1–4, pp. 241–256, Oct. 2004, doi: 10.1016/j.marchem.2004.02.014.

[62] R. A. Jahnke, "The global ocean flux of particulate organic carbon: Areal distribution and magnitude," *Global Biogeochem. Cycles*, vol. 10, no. 1, pp. 71–88, Mar. 1996, doi: 10.1029/95GB03525.

[63] X. Ran, H. Che, and T. Sun, "Distributions and sources of particle organic carbon and biogenic silica in the Bohai Sea," *Acta Oceanolog. Sin.*, vol. 36, no. 10, pp. 12–24, 2014, doi: 10.3969/j.issn.0253-4193.2014.10.002.

[64] H. Evers-King et al., "Validation and intercomparison of ocean color algorithms for estimating particulate organic carbon in the oceans," *Frontiers Mar. Sci.*, vol. 4, p. 251, Aug. 2017, doi: 10.3389/fmars.2017.00251.

[65] F. Shen, M. S. Salama, Y.-X. Zhou, J.-F. Li, Z. Su, and D.-B. Kuang, "Remote-sensing reflectance characteristics of highly turbid estuarine waters—A comparative experiment of the Yangtze river and the yellow river," *Int. J. Remote Sens.*, vol. 31, no. 10, pp. 2639–2654, May 2010, doi: 10.1080/01431160903085610.

[66] V. Vantrepotte, H. Loisel, D. Dessailly, and X. Mériaux, "Optical classification of contrasted coastal waters," *Remote Sens. Environ.*, vol. 123, pp. 306–323, Aug. 2012, doi: 10.1016/j.rse.2012.03.004.

[67] E. Aas, "Refractive index of phytoplankton derived from its metabolite composition," *J. Plankton Res.*, vol. 18, no. 12, pp. 2223–2249, 1996, doi: 10.1093/plankt/18.12.2223.

[68] H. Volten et al., "Laboratory measurements of angular distributions of light scattered by phytoplankton and silt," *Limnol. Oceanogr.*, vol. 43, no. 6, pp. 1180–1197, Sep. 1998, doi: 10.4319/lo.1998.43.6.1180.

[69] Y. Luo et al., "Saturation of water reflectance in extremely turbid media based on field measurements, satellite data and bio-optical modelling," *Opt. Exp.*, vol. 26, no. 8, p. 10435, 2018, doi: 10.1364/OE.26.010435.

[70] M. Bellacicco, J. Pitarch, E. Organelli, V. Martinez-Vicente, G. Volpe, and S. Marullo, "Improving the retrieval of carbon-based phytoplankton biomass from satellite ocean colour observations," *Remote Sens.*, vol. 12, no. 21, p. 3640, Nov. 2020, doi: 10.3390/rs12213640.

[71] H. Lyu et al., "A novel algorithm to estimate phytoplankton carbon concentration in inland lakes using Sentinel-3 OLCI images," *IEEE Trans. Geosci. Remote Sens.*, vol. 58, no. 9, pp. 6512–6523, Sep. 2020, doi: 10.1109/TGRS.2020.2977080.

[72] J. R. Graff, A. J. Milligan, and M. J. Behrenfeld, "The measurement of phytoplankton biomass using flow-cytometric sorting and elemental analysis of carbon," *Limnol. Oceanography: Methods*, vol. 10, no. 11, pp. 910–920, Nov. 2012, doi: 10.4319/lom.2012.10.910.

[73] J. R. Graff et al., "Analytical phytoplankton carbon measurements spanning diverse ecosystems," *Deep Sea Res. Part I: Oceanographic Res. Papers*, vol. 102, pp. 16–25, Aug. 2015, doi: 10.1016/j.dsr.2015.04.006.

[74] D. G. Redalje and E. A. Laws, "A new method for estimating phytoplankton growth rates and carbon biomass," *Mar. Biol.*, vol. 62, no. 1, pp. 73–79, 1981, doi: 10.1007/BF00396953.

[75] F. Shen, Y.-X. Zhou, D.-J. Li, W.-J. Zhu, and M. S. Salama, "Medium Resolution Imaging Spectrometer (MERIS) estimation of chlorophyll–A concentration in the turbid sediment-laden waters of the Changjiang (Yangtze) estuary," *Int. J. Remote Sens.*, vol. 31, nos. 17–18, pp. 4635–4650, Sep. 2010, doi: 10.1080/01431161.2010.485216.

[76] L. Zhao and L. Gao, "Dynamics of dissolved and particulate organic matter in the Changjiang (Yangtze River) estuary and the adjacent east China sea shelf," *J. Mar. Syst.*, vol. 198, Oct. 2019, Art. no. 103188, doi: 10.1016/j.jmarsys.2019.103188.

[77] C. Guo, S. Yang, W. Zhai, Y. Niu, and C. Liu, "Biological–physical oceanographic coupling influencing particulate organic matter in the south yellow sea," *Frontiers Mar. Sci.*, vol. 9, Aug. 2022, Art. no. 919423, doi: 10.3389/fmars.2022.919423.

[78] F. Shen, R. Tang, X. Sun, and D. Liu, "Simple methods for satellite identification of algal blooms and species using 10-year time series data from the east China sea," *Remote Sens. Environ.*, vol. 235, Dec. 2019, Art. no. 111484, doi: 10.1016/j.rse.2019.111484.

[79] J. Zhang, Y. Chen, and J. Yang, "Distribution of particulate amino acids in the Changjiang Estuary and its adjacent sea and their indications for degradation and sources of organic matter," *Mar. Environ. Sci.*, vol. 41, no. 2, p. 2, 2022, doi: 10.13634/j.cnki.mes.2022.02.020.

[80] H. Zhang, L. Yang, and L. Wang, "Distribution and source analyses of particulate organic carbon in the Yellow Sea and Bohai Sea during summer, 2013," *Acta Oceanolog. Sin.*, vol. 38, no. 8, pp. 24–35, 2016, doi: 10.3969/j.issn.0253-4193.2016.08.003.

[81] S. Wang et al., "Satellite estimation of suspended particle types using a backscattering efficiency-based model in the marginal seas," *Opt. Exp.*, vol. 31, no. 2, p. 890, 2023, doi: 10.1364/OE.476192.